Validation and Analysis of 3D DNS of planar pre-filming airblast atomization simulations

Anirudh Asuri Mukundan, Thibaut Ménard, A. Berlemont, Jorge César C Brändle de Motta, Ruud Eggels

ILASS-Americas 30th Annual Conference on Liquid Atomization and Spray Systems, Tempe, AZ, May 2019

Validation and Analysis of 3D DNS of planar pre-filming airblast atomization simulations

A. Asuri Mukundan[1,*], T. Ménard[1], A. Berlemont[1], J. C. Brändle de Motta[1], and R. Eggels[2]
[1]CNRS UMR6614-CORIA, Rouen, France
[2]Rolls-Royce Deutschland, Blankenfelde-Mahlow, Germany

Abstract

In this paper, results from direct numerical simulations (DNS) of published experimental configuration of planar pre-filming airblast atomization are presented. The simulations have been performed using our in-house multiphase Navier-Stokes equations solver ARCHER. The coupled level set volume of fluid (CLSVOF) method has been used for capturing the liquid/gas interface within the context of multiphase flows. This numerical method has been proved to well capture the interface from many of our previous works. A kerosene based fuel at an operating point corresponding to aircraft altitude relight conditions have been used in DNS. The results are analyzed in two parts: analysis of liquid droplets and analysis of liquid ligaments at the trailing edge of the pre-filmer plate. The analyses of the liquid droplets diameter and velocity distributions revealed that the results from the simulations are agreeing with the experimental data very satisfactorily. Moreover, the observation from these distributions is that the sheet breakup mechanism is dominant over the ligament breakup mechanism of atomization. Ligament analysis has been carried out by reducing the 3D DNS data to 1D liquid/gas interface contour. The frequency distribution of the liquid ligaments shows the under-prediction on their lengths in comparison to experiments. Overall, a satisfactory agreement has been achieved between the DNS and experiments.

*Corresponding Author: anirudh.mukundan@coria.fr

Introduction

Pre-filming planar airblast atomization involves destabilization of liquid sheet by a high speed coflowing gas stream. Such a type of atomization process is commonly employed in aircraft engines. Quite often, the velocity of the gas stream is about one order of magnitude larger than that of the liquid fuel.

With the idea of airblast atomization first introduced by Lefebvre and Miller [1], there has been multiple experimental investigations [2, 3, 4] to understand the physical processes of atomization occurring in the atomizing edge. Most of these experimental analyses focused on the far downstream properties such as droplet diameter and velocity distribution analysis. But the characteristics of atomization near the pre-filmer plate have not been extracted from experiments. The work of Bilger and Stewart Cant [5] focused on the airblast atomization and regime classification for different gas and liquid phase velocities. This work used laminar velocity profile for the phases thus might not necessarily represent the real time fuel injection scenarios. In the past years, multiple works on airblast atomization using numerical simulations are performed, such as, Fuster et al. [6] studied the primary break up of planar coflowing sheets of water and air at dynamic pressure ratios of 0.5 to 32; Chiodi et al [7] studied the cylindrical and planar airblast atomization using semi-Lagrangian geometric VOF method and accurate conservative level set (ACLS) method and showed the cascade of instabilities from Kelvin-Helhmholtz to Rayleigh-Taylor to Rayleigh-Plateau in the breakup mechanism; and Agbaglah et al [8] studied the destabilization of the air/water planar liquid sheet and found excellent agreement between experiments and simulations for liquid cone length, spatial growth of primary instability, and maximum wave frequency. A recent work by Braun et al [9] used meshless smoothed particle hydrodynamics (SPH) for numerically predicting the air-assisted atomization and compared their results with that from the work of Gepperth et al [10].

Recently, the works of Gepperth et al [10] and Warncke et al [11] on planar pre-filming airblast atomization extracted experimentally and numerically the information close to the plate such as ligament lengths and deformation velocity. Although a good agreement between experiments and simulations had been observed in the work of Warncke et al [11], the results displayed the limitation of the diffused interface capturing methods used in their simulations. Thus, to this end, in our work we have used direct numerical simulations (DNS) approach to simulate the planar pre-filming airblast atomization for same operating point and configuration as described in Warncke et al [11] and compare the results with the experimental work of Gepperth et al [10]. In contrast to Warncke et al [11], we use a sharp interface capturing method called coupled level set volume of fluid (CLSVOF) method [12] for accurately capturing the liquid/gas interface.

This paper is organized as follows. First, we present the governing equations of the flow that are solved in our in-house flow solver ARCHER [12, 13]. Then a brief presentation of the numerics behind the CLSVOF method is given. Next, we present the configuration and computational setups of our airblast atomization. Results on the liquid droplets and liquid ligament characteristics from the simulations are then presented and compared with the experimental data. Finally, concluding remarks are drawn based on the presented results.

Governing Equations

The solver used in this study is ARCHER, whose capabilities are described extensively in multiple works [12, 13, 14]. This solver is structured, parallel and developed for direct numerical simulations (DNS) of complex and turbulent multiphase flows with the application to study primary breakup of liquid fuel jet. A staggered variable configuration is used with central finite difference scheme for least numerical dissipation.

The pressure and velocity fields describing the flow are obtained by solving the incompressible Navier–Stokes equations. The following form of the Navier–Stokes equations are solved in ARCHER:

$$\boldsymbol{\nabla} \cdot \boldsymbol{u} = 0, \tag{1}$$

$$\frac{\partial \rho \boldsymbol{u}}{\partial t} + \boldsymbol{\nabla} \cdot (\rho \boldsymbol{u}\, \boldsymbol{u}) = -\boldsymbol{\nabla} P + \boldsymbol{\nabla} \cdot (2\mu \boldsymbol{D}) + \boldsymbol{B}, \tag{2}$$

where $\boldsymbol{u}$ is the velocity field, P is the pressure field, μ is dynamic viscosity, ρ is density, $\boldsymbol{D}$ is the strain rate tensor given as $\boldsymbol{D} = \frac{1}{2}(\boldsymbol{\nabla u} + (\boldsymbol{\nabla u})^T)$, and $\boldsymbol{B}$ is the sum of the body and surface tension forces. $\boldsymbol{B} = \boldsymbol{B}_{\mathrm{b}} + \boldsymbol{B}_{\mathrm{st}}$ where $\boldsymbol{B}_{\mathrm{b}}$ is the force due to gravity and $\boldsymbol{B}_{\mathrm{st}}$ is the force due to surface tension which is given as $\boldsymbol{B}_{\mathrm{st}} = \sigma \kappa \delta_I \boldsymbol{n}$. σ represent the surface tension, κ is the curvature of the interface computed using the liquid/gas interface unit normal $\boldsymbol{n}$ as $\kappa = \boldsymbol{\nabla} \cdot \boldsymbol{n}$, and δ_I is the Dirac delta function centered on it. A consistent mass and momentum flux computation [13] is employed.

A projection method as described in Ménard et al [12] is employed for solving Equations (1) and (2). A 2$^{\mathrm{nd}}$ order central difference scheme is employed for discretization of the spatial derivatives to avoid any dissipation. However, the convection term is dis-

cretized using 5^{th} order WENO scheme to ensure a robust behavior of the solution. A consistent mass and momentum flux computation [13] is employed. The viscous term is discretized following the method described in Sussman et al [15]. Ghost Fluid Method (GFM) [16] is employed for the spatial discretization of the Poisson equation for taking into account the force due to surface tension as a pressure jump. The resulting linear system of symmetric and positive definite matrix with five diagonals is solved using multigrid algorithm for preconditioning a conjugate gradient (CG) method [14]. The temporal derivatives in this study are discretized using one-step forward Euler scheme.

CLSVOF Method

A coupled level set volume of fluid (CLSVOF) method of Ménard et al [12] is used for capturing the liquid/gas interface. The details of this method are briefly presented in the following subsections.

Level Set

The backbone of the CLSVOF method is the level set function ϕ the basis of which has been proposed by Osher and Sethian [17]. This function is a signed distance function (i.e., $\phi > 0$ in liquid phase regions and $\phi < 0$ in gas phase regions of the simulation domain) defined as the algebraic distance between any point of the domain and the interface. The liquid/gas interface is then represented as the zero-level of this level set function. The advantage of this function is the ease of computation of geometric quantities pertaining to the interface. For example, the interface unit normal is computed as

$$\boldsymbol{n} = \frac{\boldsymbol{\nabla}\phi}{\|\boldsymbol{\nabla}\phi\|_2}, \tag{3}$$

and interface curvature κ is computed as

$$\kappa = \boldsymbol{\nabla} \cdot \boldsymbol{n}. \tag{4}$$

The advection of the level set function is performed by solving the following transport equation.

$$\frac{\partial \phi}{\partial t} + \boldsymbol{\nabla} \cdot (\phi \boldsymbol{u}) = 0 \tag{5}$$

One of the problems that arise when solving this equation is that, due to the wide spreading and stretching of the level set in the numerical simulation domain, the level set function will no longer satisfy the condition of $\|\boldsymbol{\nabla}\phi\|_2 = 1$. Thus, a redistancing procedure [18] is required to ensure the satisfaction of this condition and keep ϕ as the algebraic distance function.

Coupling Level Set and Volume of Fluid

The combined procedure of solving Equation (5) and redistancing can create loss of mass in the numerical domain especially when reconstructing interface for under-resolved liquid structures. In order to solve this problem, the level set method is coupled with a classical volume of fluid [19, 20]. This coupling is performed similar to the work of Sussman and Puckett [21] the details of which are explained in Ménard et al [12]. The main differences with the CLSVOF method consist in keeping the initial re-distancing algorithm in our approach, and we modified the reconstruction technique to define the interface in a cell from the level set position.

With regards to the reconstruction of the liquid/gas interface, a PLIC method is used. Thus, a linear interface is used as an approximation of the original/reference interface. Hence, the equation of the interface in 3D is $ax+by+cz+d = 0$ where the interface unit normal $\boldsymbol{n} = [a, b, c]^T$ and d is the shortest distance of the interface from the center of each computational cell. The computation of the components of the unit normal is determined from the level set signed distance function. In the CLSVOF method, the computation of the variable d, defining the shortest distance of the interface from the cell center, is performed by satisfying the volume conservation condition, i.e.,

$$\left\| F^{\text{ref}} - F^{\text{act}}(\boldsymbol{n}, d) \right\|_2 = 0, \tag{6}$$

using Newton-Raphson method upto the machine precision. In this condtion, F represent the liquid volume fraction and the superscript "ref" correspond to the original/reference interface while "act" correspond to reconstructed/actual interface. The idea of solving the above equation is to perform interface reconstruction by conserving the liquid volume in the numerical simulation domain. For more details, the reader is referred to Ménard et al [12].

Case Setup

A planar pre-filming airblast atomizer configuration is considered in this work. Figure 1a represents a geometry simplification of the annular atomizer used in our Direct numerical simulations (DNS). This simplified geometry is inspired from the work of Warncke et al [11].

Operating Conditions

Fuel injection in aircraft engines are characterized by high Reynolds and Weber number. A detailed investigation of fuel injection in such highly turbulent environment is challenging using DNS. A moderate operating point is thus chosen with a com-

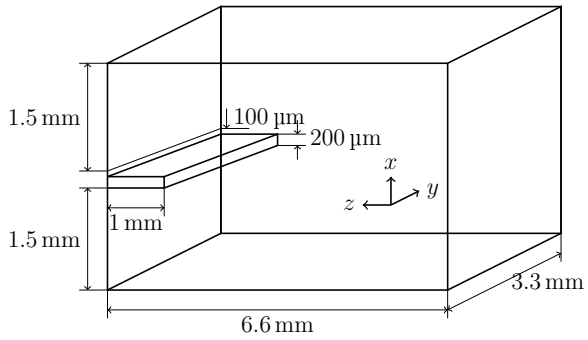

(a) DNS computational domain

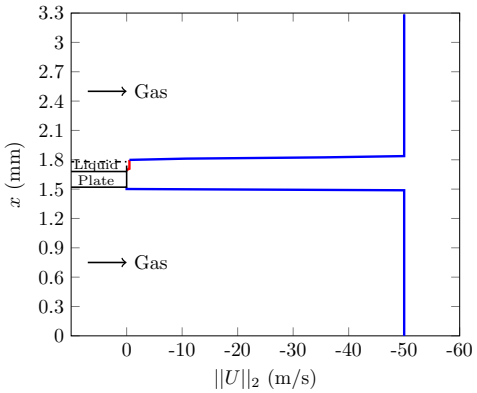

(b) Velocity profile for liquid and gas phases

Figure 1: DNS Domain (a) and inflow phase velocity profile (b): liquid phase (——); gas phase (——). Negative velocity is due to downstream direction oriented along negative $z-$direction.

paritively low Reynolds and liquid film Weber number. This operating point correspond to the aircraft altitude relight conditions [22] and allows an adequate resolution of the atomization events. The operating conditions are summarized in Table 1 with channel half width $H_{\text{chw}} = 4\,\text{mm}$ and liquid film thickness $h_{\text{l}} = 100\,\mu\text{m}$. The liquid fuel used in this study correspond to Shellsol D70 with a low surface tension at ambient conditions.

Computational Setup

The air flow inlet is located each above and below the pre-filmer plate. A flat velocity profile as shown in Figure 1b with the magnitude of the mean liquid and gas phase velocity is imposed as the inlet profile. A thickness 25.7 µm has been considered for gas boundary layer over liquid when imposing the velocity profile. The turbulence is initiated in the simulation using the method of Klein et al [23]. The DNS domain has been chosen in such a way that there is enough length along the downstream direction to analyze atomization but also kept as small as possible to avoid blow up of the computational cost.

The faces of the pre-filmer plate are treated as walls using the staircase immersed boundary method (SIBM). In this method, the shape of the pre-filmer plate is approximated such that it fits in the Cartesian grid lines. Thus, fluxes over the cell faces containing the solid pre-filmer plate can be computed like that for a no-slip boundary cell face. Periodic boundary conditions have been used along the $y-$direction, while outflow boundary conditions on all other directions except the liquid and gas injection $z-$plane.

A computational mesh with a mesh spacing of $\Delta x = \Delta y = \Delta z = 12.89\,\mu\text{m}$ has been employed to capture the liquid droplets resulting in a total of 33.5 million cells. For the value of Reynolds number employed in this study, the Kolmogorov length scale was found to be $\eta = 12\,\mu\text{m}$. Thus, based on [24], the required minimum grid spacing is $\Delta x_{\text{min}} \approx 25\,\mu\text{m}$. With the grid resolution used in this work, it can be said that we will be able to resolve the predominant scales of motion. The simulation has been run upto a physical time of 8.77 ms on 1024 processors in CRIANN supercomputing facility.

Experimental Comparison

In order to validate the results from DNS, we will be comparing with the experimental data from the work done at the Institut für Thermische Strömungsmaschinen (ITS) at Karlsruhe Institut für Technologie. The experiments have been performed for 30 s of physical time and 300 double frame images (in both $y-z$ and $x-z$ plane views) that are phase shifted by 10 µs are obtained every 0.1 s. Each droplet in the double image was considered for the computation of statistics. To statistically derive robust results for the ligament and droplet sizes, an efficient algorithm based on the particle and ligament tracking velocimetry developed by Müller [25] with an extension to Depth of Field (DoF) correction to increase the measurement accuracy was used. For more details on the measurement and post-processing techniques employed in the experimental work, the reader is referred to [10, 11].

Results and Discussion

In this section, the results from post-processing of the DNS data are presented. First, the qualitative results of the flow visalization are presented. Then the quantitative results on the droplets and ligaments are presented.

Table 1: Operating Conditions Summary

Liquid properties	$\overline{u}_\mathrm{l} = 0.5\,\mathrm{m/s}$	$\rho_\mathrm{l} = 770\,\mathrm{kg/m^3}$	$\nu_\mathrm{l} = 2.03 \times 10^{-6}\,\mathrm{m^2/s}$
	$\sigma = 0.0275\,\mathrm{kg/s^2}$		
Gas properties	$\overline{u}_\mathrm{g} = 50\,\mathrm{m/s}$	$\rho_\mathrm{g} = 1.2\,\mathrm{kg/m^3}$	$\nu_\mathrm{g} = 1.5 \times 10^{-5}\,\mathrm{m^2/s}$
Non-dimensional num.	$\mathrm{Re_g} = \frac{\overline{u}_\mathrm{g} H_\mathrm{chw}}{\nu_\mathrm{g}} = 13\,333$	$\mathrm{We_l} = \frac{\rho_\mathrm{g}(\overline{u}_\mathrm{g} - \overline{u}_\mathrm{l})^2 h_\mathrm{l}}{\sigma} = 10.69$	$M = \frac{\rho_\mathrm{g} \overline{u}_\mathrm{g}^2}{\rho_\mathrm{l} \overline{u}_\mathrm{l}^2} = 15.58$

Qualitative results

Figure 2 shows several instantaneous snapshots of the flow visualization. Two distinct mechanisms of breakup can be observed: first, the sheet breakup and second, the ligament breakup. The waves generated on top of the liquid layer by the high speed flowing air forms a thin sheet at the trailing edge of the pre-filmer plate (c.f. Figure 2a). This liquid sheet then develop holes (c.f. Figure 2b) which penetrate thereby leading to breakup into small droplets that are of the size of the thickness of the sheet. As the simulation is progressed, we observe another mechanism of breakup, namely ligament breakup. Due to the high difference between the velocity of liquid and gas, an accumulation of liquid occurs at the trailing edge of the pre-filmer plate (c.f. Figure 2d). This then form long thin ligament-like structures which then subsequently breaks up into medium sized droplets (c.f. Figure 2f). This observation is consistent with the torn sheet breakup regime described by Fernández et al [26] for the operating point in this work. It is to be remarked that there was no observation of dewetting of the plate found in the simulations. Furthermore, Figures 3 and 4 present the rendered images from the DNS displaying the sheet and ligament breakup mechanism forming small and medium sized droplets respectively. Figure 5 shows a rendered image at a time instant in the simulation with the presence of large number of droplets of different sizes formed from the breakup of sheet and ligaments.

Quantitative results

Now, the quantitative data obtained from post-processing and analysis of the data from DNS are presented and compared with the experimental results. This subsection first presents the post-processing techniques employed for the DNS data that is consistent to that of the experiments. It is then followed by the characterization of the droplets and ligaments that include presentation of their probability distributions and also their mean values.

Post-processing Techniques

The post-processing and analysis of the DNS data is split into two parts: analysis of droplets and analysis of accumulated liquid ligaments at the trailing edge of the pre-filmer plate.

In order to determine the probability distribution of the droplets in the domain, a connected component labelling (CCL) algorithm is used. This algorithm finds list of all the liquid structures in the domain at a given time instant by using a 8-cell neighbor connectivity search for liquid presence. This list contains all the attributes of the liquid structures such as velocity components, surface area, diameter, and volume. It is to be remarked that the liquid droplet structure diameter is derived from its volume with the assumption that liquid structure is spherical.

The extraction of results for the liquid ligaments accumulated at the trailing edge of the pre-filmer plate such as ligament lengths and breakup length is challenging. To this end, we have used an algorithm that is split into four steps. First, the 3D DNS data (c.f. Figure 6a) is reduced to a 2D data analogous to the shadowgraphy images by assigning label value of 0 (for gas) and 1 (for liquid) to each cell with zero and non-zero liquid volume fraction respectively. Second, these label values are summed up along cross-stream $x-$direction to generate a projected top view ($y-z$ plane view) (c.f. Figure 6b). Any cell in this top view with a summed label value greater than 1 indicates presence of liquid in this view. Third, a CCL algorithm is applied for these summed up label values to identify the biggest liquid structure, i.e., the accumulated liquid at the trailing edge of pre-filmer plate (c.f. Figure 6c). Finally, the 1D interface contour is identified using the method described in [27, 28] that characterizes the interface of this accumulated liquid (c.f. Figure 6d). This procedure has been applied to every time step since the first breakup event has occurred.

Droplet characterization

With the post-processing technique described above, first the droplet characteristics are extracted from the DNS. These include droplet diameter and

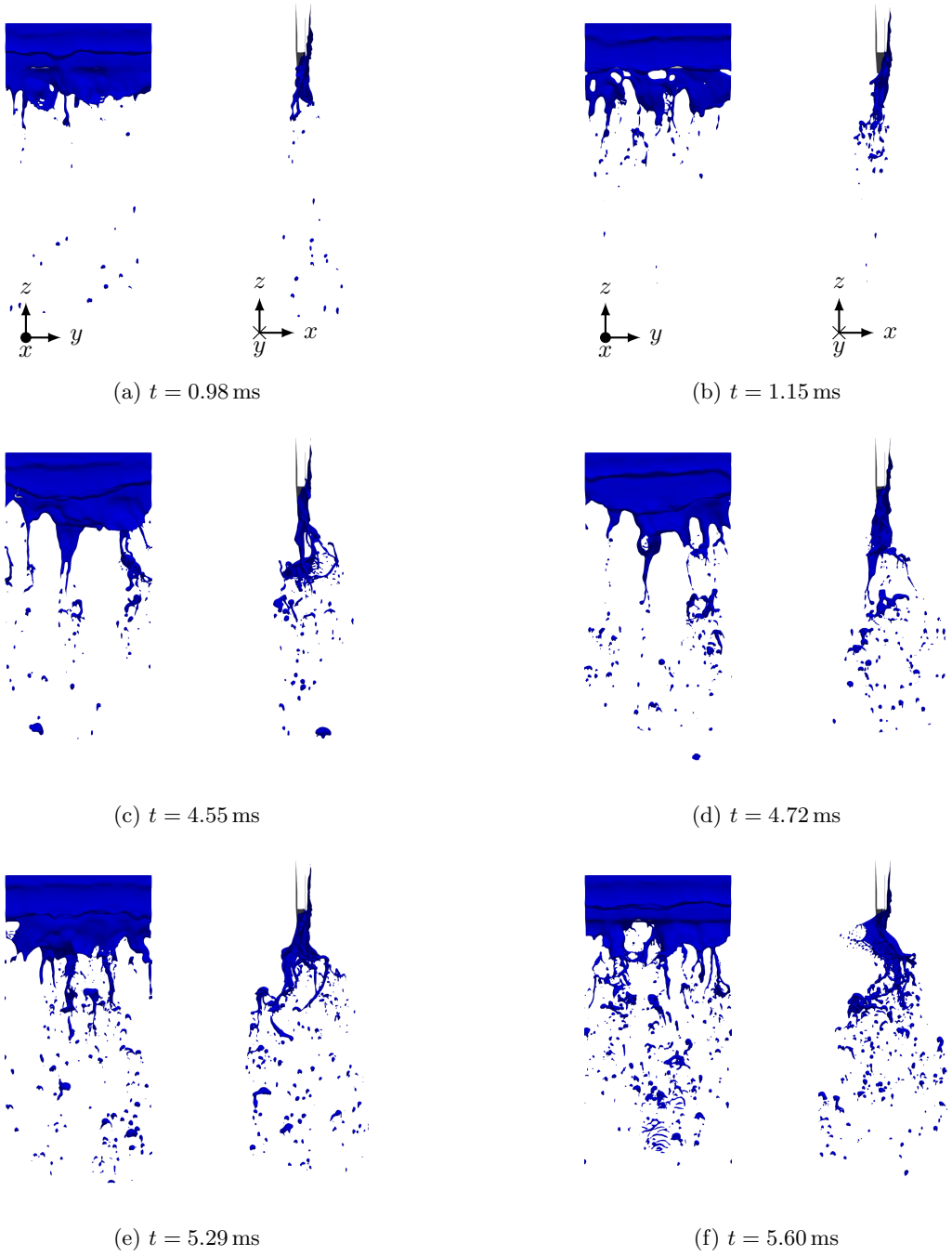

(a) $t = 0.98\,\text{ms}$ (b) $t = 1.15\,\text{ms}$

(c) $t = 4.55\,\text{ms}$ (d) $t = 4.72\,\text{ms}$

(e) $t = 5.29\,\text{ms}$ (f) $t = 5.60\,\text{ms}$

Figure 2: Atomization of liquid fuel at the trailing edge of pre-filmer plate forming ligaments and droplets.

droplet streamwise velocity (w_z) distributions shown in Figure 7. The liquid packets are obtained for each time step from the whole DNS domain. In order to have single count of a liquid packet/droplet, we developed an algorithm that tracks the position of each droplet between adjacent time steps (t^n and t^{n+1}, for example) and adds to the list of droplets for distribution plot only when it goes out of the domain at t^{n+1}. The smallest diameter measured in the experiment was 15 µm, while that from the simulation is 28 µm which is about $2.5\Delta x$. From Figure 7, a satisfactory agreement between the simulation and experiments is observed with under-prediction from the simulation. A profile similar to that of the

Figure 3: Liquid sheet breakup displayed in rendered image from the DNS at $t = 1.51\,\text{ms}$. Thin sheet formation at the trailing edge of pre-filmer plate with holes subsequently breaking into small droplets of the thickness of the sheet.

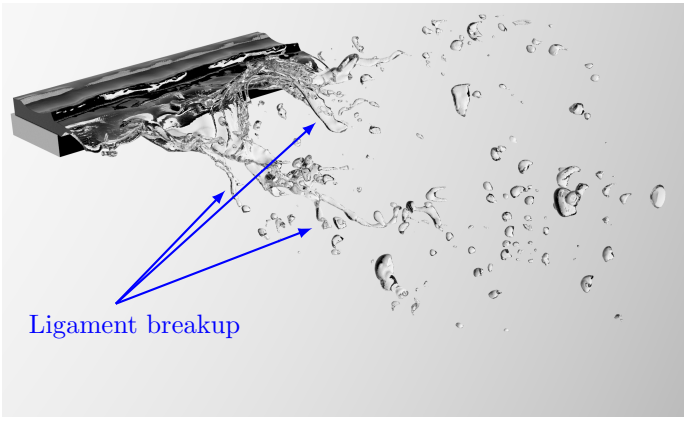

Figure 4: Liquid ligament breakup displayed in rendered image from the DNS at $t = 1.51\,\text{ms}$. Formation of long thin irregular shaped ligament breaking up into medium sized droplets.

Figure 5: Rendered image displaying the formation of large number of varying sized droplets broken up from liquid sheet and ligaments.

experiments but with under-prediction of probability is observed from the simulations. Droplet diameters upto $254\,\mu\text{m}$ are found from the DNS. As seen in qualitative results subsection, a large num-

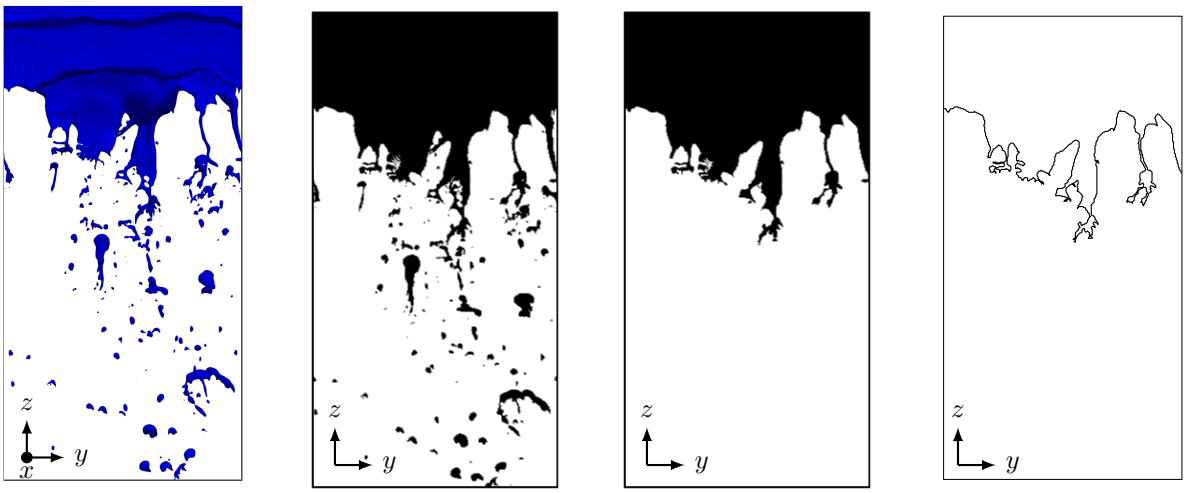

(a) 3D DNS data (b) 2D Projected DNS data (c) Biggest liquid structure (d) 1D phase interface

Figure 6: Reduction of 3D to 1D data for computing ligament characteristics for $t = 5.05\,\text{ms}$.

ber of small droplets are found thus owing to the higher peak for the small sized droplets . Additionally, we can see a similar multimodal distribution of the droplet diameters with peaks centered at 25 µm (small droplets), 57 µm (medium sized droplets) and 120 µm (large droplets). The highest peak of the diameter distribution is observed for small droplet diameters. As explained in previous subsection, such small droplets are produced from the sheet breakup mechanism. Since the magnitude of the peak for smaller droplets are relatively higher than those for larger droplet diameters, we can conclude that the sheet breakup mechanism is dominant over ligament breakup mechanism in the simulations. This observation is consistent with that from experiments. Moreover, this could also be attributed to the flat inflow velocity profile chosen in our study for the liquid and gas phase. The investigation of the effect of inlet velocity profile on the droplet characteristics is considered as future work in our project.

The droplet velocity distribution shown in Figure 7b displays a good agreement with the mean velocity from the experiment measured as 14.5 m/s while that from the simulation is 16 m/s. Moreover, the trend in the profile of the distribution function is similar to that of the experiments. A total of 2503 droplets were identified after post-processing the DNS data for simulations run upto 8.77 ms. In contrast, about 38 000 droplets were identified from the experiments for a measurement duration of 30 s. Moreover, the experimental setup had larger domain and measurements were taken for longer physical time than in our simulations thereby owing to observation of larger number of droplets. To get deeper insights into the droplet properties, a scatter plot of the streamwise droplet velocity and droplet diameter is shown in Figure 7c for all droplets. It can be seen that there are small droplets with high velocity of 45 m/s are present in the domain. This observation is consistent with the experiments [11]. Finally, the Sauter Mean Diameter (SMD) computed from the DNS is 103.68 µm. This shows good agreement with the value found from the experiment of 154.8 µm.

Ligament characterization

The ligaments are formed in irregular shapes at the trailing edge of the pre-filmer plate. The characterization of these ligaments are performed using computation of ligament lengths and breakup length. To this end, the accumulated liquid at the trailing edge of pre-filmer plate is under focus. The method explained in Warncke et al [11] is used for the experiments while the technique employed for post-processing our DNS data is explained below.

A single ligament length l_{lig} is defined, within this work, as the distance between the ligament peak and the trailing edge of the pre-filmer. To compute the ligament length for a single time step, the 1D phase interface contour is used. The maximum dip in this 1D phase interface along the downstream direction is used for identifying the ligaments. The critical point in this identification is to compute the true ligament length by eliminating the effect of the wrinkling in the interface. For this reason, following [11], we use a criterium of 50 µm distance between the adjacent minima and maxima measured along the streamwise $z-$direction is kept as a threshold to eliminate this effect and obtain a more global be-

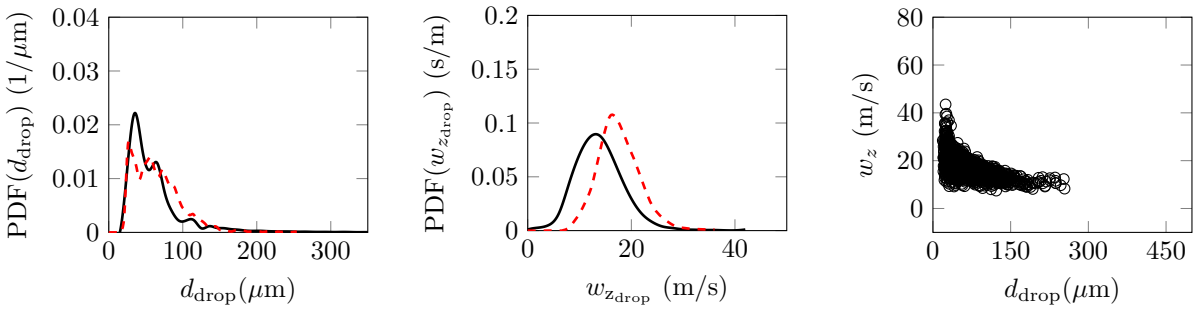

(a) Droplet size distribution

(b) Droplet velocity distribution

(c) Scatter plot of droplet velocity and diameters

Figure 7: Characterization of droplets: Experiments (——) and DNS (- - -).

havior. This is shown in Figure 8 with the squares indicating the location of the maximum dip in the interface in the downstream direction. The length of these resulting maximum dips (called true ligament lengths hereon) are computed from the edge of the pre-filmer plate. The breakup length l_{breakup} is then defined as the mean of these true ligament lengths over all time steps.

Based on these computations, the breakup length from the DNS is found to be $l_{\text{breakup}} = 1.17\,\text{mm}$ while the experimental value measures 3.2 mm. The breakup length from the simulations are smaller in magnitude albeit of the same order as that of the experimental value. Per the study of Sauer et al [29], when the breakup length is computed as the maximum of all the ligament lengths, the result from our simulation is 3.74 mm which is only a little over-prediction in comparison to the experiments. In experiments, a small amount of ligaments whose lengths measures greater than the length of the streamwise direction in the DNS are observed which results in a greater breakup lengths. Furthermore, a total of 1657 ligaments have been identified from the DNS post-processing while 13 000 ligaments from the experiments. This vast difference in the total number of ligaments between experiments and simulations is attributed to two factors: larger domain and long time of measurement in experiments.

To get a better understanding, frequency distribution of ligament length is computed and shown in Figure 9. It can be seen that the peak of this ligament length distribution is shifted towards smaller lengths. This is due to three reasons: first, no ligaments measured from our simulations reaches the outlet of the domain; second, there was greater time period for the sampling in the experiments, and therefore, a higher amount of samples compared to the simulations; and third, the field of view of measurement for experiments are larger than that of the DNS, thus, longer ligament lengths that are greater than the length of the streamwise direction of the DNS domain are observed. Furthermore, these under-predictions could be attributed to the insufficiency of the mesh resolution to capture the breakup events.

Conclusions

Results from the DNS of planar pre-filming airblast atomization have been presented. The coupled level set volume of fluid (CLSVOF) method is used for capturing the liquid/gas interface in the simulations. The operating conditions of the simulations correspond to aircraft altitude relight conditions. The analysis of the DNS data is split into analysis of droplets and analysis of ligaments. A satisfactory agreement has been observed between DNS and experiments for the droplet diameter distribution while a good agreement has been observed for the droplet streamwise velocity distribution. Furtheremore, the value of the Sauter Mean Diameter (SMD) droplet from the DNS were found to be in close agreement with the experimental value. Moreover, the observation from these distributions is that the sheet breakup mechanism is dominant over the ligament breakup mechanism of atomization. The analysis of the ligaments involved projection of the 3D DNS data into a plane and finding a 1D liquid/gas interface contour. The results from this analysis revealed that there is an under-prediction on the frequency distribution of the ligament lengths from the simulations in comparison to the experiments. This is attributed to: insufficiency in the mesh resolution and long measurement time and detection of more ligaments in the experiments. Furtheremore, this under-prediction could also be attributed to the inlet velocity profile imposed for the

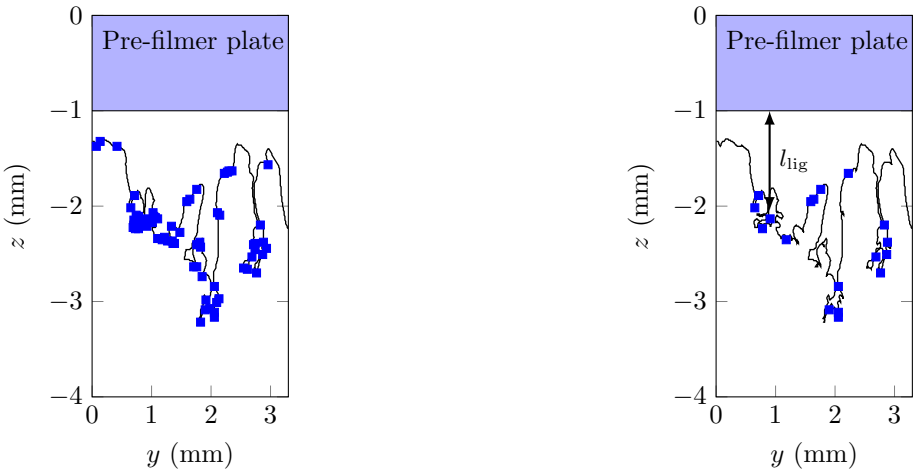

(a) All identified maxima

(b) True maxima after 50 µm criterium

Figure 8: Detection of phase interface peak (blue squares) for ligament length computation.

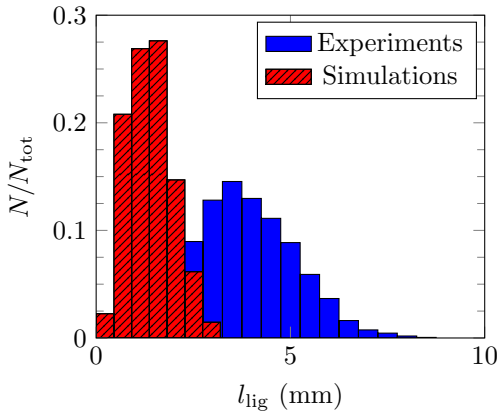

Figure 9: Frequency distribution of ligament length.

liquid and gas phase.

In future, it is envisaged to perform DNS for finer mesh resolution to capture the breakup physics and capture the small droplets. Additionally, usage of a larger DNS domain and a more realistic velocity profile for the phases such as a fully developed turbulent channel flow profile are considered in the next studies.

Acknowledgements

The funding for this project from the European Union's Horizon 2020 research and innovation programme under the Marie Skłodowska-Curie grant agreement N° 675676 is gratefully acknowledged. The computing time at CRIANN (Centre Régional Informatique et d'Applications Numériques de Normandie) under the scientific project No. 2003008 is also gratefully acknowledged. The authors would like to thank Prof. Dr. Jean-Bernard Blaisot for graciously sharing his algorithm of finding the 1D interface contour. The authors wish to thank Prof. Rainer Koch and his group at Institut für Thermische Strömungsmaschinen in Karlsruher Institut für Technologie (KIT), Germany for graciously sharing their experimental data. The authors wish to express their gratitude to Dr. Fabien Thiesset for blender image rendering tutorial and beginner scripts.

References

[1] A. H. Lefebvre and D. Miller. The development of an air blast atomizer for gas turbine application. Technical Report AERO No. 193, The College of Aeronautics Cranfield, 1966.

[2] J. C. Lasheras, E. Villermaux, and E. J. Hopfinger. *Journal of Fluid Mechanics*, 357:351–379, February 1998.

[3] U. C. Bhayaraju and C. Hassa. *Atomization and Sprays*, 19(12):1147–1169, 2009.

[4] A. K. Jasuja. *Proceedings of the 10th ICLASS, 27th August–1st September, Kyoto, Japan*, 2006.

[5] C. Bilger and R. Stewart Cant. *Proceedings of the 27th Annual Conference on Liquid Atomization and Spray Systems, 4-7 September 2016, Brighton, UK*, 2016.

[6] D. Fuster, J.-P. Matas, S. Marty, S. Popinet, J. Hoepffner, A. Cartellier, and S. Zaleski. *Journal of Fluid Mechanics*, 736:150–176, December 2013.

[7] R. Chiodi, G. Agbaglah, and O. Desjardins. *ILASS Americas 28th Annual Conference on Liquid Atomization and Spray Systems, Dearborn, MI, May*, 2016.

[8] G. Agbaglah, R. Chiodi, and O. Desjardins. *Journal of Fluid Mechanics*, 812:1024–1038, 2017.

[9] S. Braun, L. Weith, S. Holz, T. F. Dauch, M. C. Keller, G. Chaussonnet, S. Gepperth, R. Koch, and H.-J. Bauer. *International Journal of Multiphase Flow*, 2019 (in press accepted manuscript).

[10] S. Gepperth, A. Müller, R. Koch, and H.-J. Bauer. *Proceedings of the ICLASS 2012, 12th Triennial International Conference on Liquid Atomization and Spray Systems, Heidelberg, Germany, September 2-6, 2012*, 2012.

[11] K. Warncke, S. Gepperth, B. Sauer, A. Sadiki, J. Janicka, R. Koch, and H.-J. Bauer. *International Journal of Multiphase Flow*, 91:208–224, 2017.

[12] T. Ménard, S. Tanguy, and A. Berlemont. *International Journal of Multiphase Flow*, 33(5):510–524, 2007.

[13] G. Vaudor, T. Ménard, W. Aniszewski, M. Doring, and A. Berlemont. *Computers & Fluids*, 152:204–216, 2017.

[14] S. Tanguy and A. Berlemont. *International Journal of Multiphase Flow*, 31:1015–1035, 2005.

[15] M. Sussman, K. M. Smith, M. Y. Hussaini, M. Ohta, and R. Zhi-Wei. *Journal of Computational Physics*, 221(2):469–505, 2007.

[16] R. Fedkiw, T. Aslam, B. Merriman, and S. Osher. *Journal of Computational Physics*, 152(2):457–492, July 1999.

[17] S. Osher and J. A. Sethian. *Journal of Computational Physics*, 79(1):12–49, November 1988.

[18] M. Sussman, E. Fatemi, P. Smereka, and S. Osher. *Computers & Fluids*, 27(5–6):663–680, June 1998.

[19] E. Aulisa, S. Manservisi, R. Scardovelli, and S. Zaleski. *Journal of Computational Physics*, 192(1):355–364, 2003.

[20] W. Aniszewski, T. Ménard, and M. Marek. *Computers & Fluids*, 97:52–73, 2014.

[21] M. Sussman and E. G. Puckett. *Journal of Computational Physics*, 162,:301–337, 2000.

[22] T. Mosbach, R. Sadanandan, W. Meier, and R. Eggels. *Proceedings of the ASME Turbo Expo 2010: Power for Land, Sea, and Air, Volume 2: Combustion, Fuels and Emissions, Parts A and B, Glasgow, UK, June 14–18, 2010*, volume 2, 2010.

[23] M. Klein, A. Sadiki, and J. Janicka. *Journal of Computational Physics*, 186(2):652–665, April 2003.

[24] S. B. Pope. *Turbulent Flows*. Cambridge University Press, 2000.

[25] A. Müller. PhD thesis, Institut für Thermische Strömungsmaschinen (ITS), Karlsruhe Institut für Technologie, 2015.

[26] V. G. Fernández, P. Berthoumieu, and G. Lavergne. *Comptes Rendus Mécanique*, 337(6–7):481–491, November 2009.

[27] N. Fdida and J.-B. Blaisot. *ISFV13–13th International Symposium on Flow Visualization, FLUVISU12 - 12th French Congress on Visualization in Fluid Mechanics July 1-4, 2008, Nice, France*, 2008.

[28] J.-B. Blaisot. *14th ICLASS, July 22-26, Chicago, USA*, 2018.

[29] B. Sauer, A. Sadiki, and J. Janicka. *Atomization and Sprays*, 26(3):187–217, 2016.